Enhanced Piezoelectric Response of AlN via CrN Alloying

Sukriti Manna,[1] Kevin R. Talley,[2,3] Prashun Gorai,[2,3] John Mangum,[2] Andriy Zakutayev,[3] Geoff L. Brennecka,[2] Vladan Stevanović,[2,3] and Cristian V. Ciobanu[1,*]

[1]*Department of Mechanical Engineering, Colorado School of Mines, Golden, Colorado 80401, USA*
[2]*Department of Metallurgical and Materials Engineering, Colorado School of Mines, Golden, Colorado 80401, USA*
[3]*National Renewable Energy Laboratory, Golden, Colorado 80401, USA*

(Received 17 August 2017; revised manuscript received 12 February 2018; published 26 March 2018)

Since AlN has emerged as an important piezoelectric material for a wide variety of applications, efforts have been made to increase its piezoelectric response via alloying with transition metals that can substitute for Al in the wurtzite lattice. We report on density functional theory calculations of structure and properties of the $Cr_xAl_{1-x}N$ system for Cr concentrations ranging from zero to beyond the wurtzite-rocksalt transition point. By studying the different contributions to the longitudinal piezoelectric coefficient, we propose that the physical origin of the enhanced piezoelectricity in $Cr_xAl_{1-x}N$ alloys is the increase of the internal parameter u of the wurtzite structure upon substitution of Al with the larger Cr ions. Among a set of wurtzite-structured materials, we find that $Cr_xAl_{1-x}N$ has the most sensitive piezoelectric coefficient with respect to alloying concentration. Based on these results, we propose that $Cr_xAl_{1-x}N$ is a viable piezoelectric material whose properties can be tuned via Cr composition. We support this proposal by combinatorial synthesis experiments, which show that Cr can be incorporated in the AlN lattice up to 30% before a detectable transition to rocksalt occurs. At this Cr content, the piezoelectric modulus d_{33} is approximately 4 times larger than that of pure AlN. This finding, combined with the relative ease of synthesis under nonequilibrium conditions, may position $Cr_xAl_{1-x}N$ as a prime piezoelectric material for applications such as resonators and acoustic wave generators.

DOI: 10.1103/PhysRevApplied.9.034026

I. INTRODUCTION

Aluminum nitride has emerged as an important material for microelectromechanical-based systems (MEMSs) [1,2] such as surface and bulk acoustic resonators [1,3], atomic force microscopy cantilevers [1], accelerometers [4,5], oscillators [6], resonators for energy harvesting [7,8], and bandpass filters [9]. The advantages of using AlN in MEMS devices include CMOS compatibility, high thermal conductivity, and high temperature stability. In addition, its low permittivity and high mechanical stiffness are particularly important for resonantor applications [1,10]. However, the piezoelectric constants of AlN thin films are lower than those of other commonly used piezoelectric materials. For example, the out-of-plane piezoelectric strain modulus d_{33} [11] of reactively sputtered AlN films is reported to be 5.5 pC/N, whereas the d_{33} value for ZnO can be at least twice as large [12], and lead zirconate-titanate films can be over 100 pC/N [2].

It is therefore desirable to find ways to increase the piezoelectric response of AlN in order to integrate AlN-based devices into existing and future systems. A common way to engineer piezoelectric properties of AlN is by alloying with transition-metal nitrides (Sc, Y, and others), which can lead to a severalfold increase in the field-induced strain via increases in the longitudinal piezoelectric coefficient e_{33} and simultaneous decreases in the longitudinal elastic stiffness C_{33} [13–16]. In the case of ScN alloying, the origins of this response have been studied [16], and it is presumed that other such systems which also involve AlN alloyed with rocksalt-structured end members are similar: as the content of the rocksalt end member in the alloy increases, the accompanying structural frustration enables a greater piezoelectric response. This structural frustration, however, is also accompanied by thermodynamic driving forces for phase separation [17] which, with an increased alloy concentration, lead to the destruction of the piezoelectric response upon transition to the (centrosymmetric, cubic) rocksalt structure. The experimental realization of large alloy contents without phase separation or severe degradation of film texture and crystalline quality can be quite difficult [17,18], even when using nonequilibrium deposition processes such as sputtering. Thus, it is desirable to find alloy systems for which the structural transition from wurtzite to rocksalt occurs at low alloying concentrations since these alloys may be more easily synthesized and more

*Corresponding author.
cciobanu@mines.edu

 © 2018 American Physical Society

stable, while they also (hypothetically) provide property enhancements comparable to those observed in the more-studied $Sc_xAl_{1-x}N$ alloy system. Among the AlN-based systems presently accessible experimentally, $Cr_xAl_{1-x}N$ has the lowest transition composition between the wurtzite and rocksalt structures, occurring at approximately 25% CrN concentration [19,20]. This transition point comparison motivates the investigation of the piezoelectric properties of the $Cr_xAl_{1-x}N$ system, which we also refer to, for simplicity, in terms of Cr substitution for Al.

In this article, we study Cr-substituted AlN using density functional theory (DFT) calculations of structural, mechanical, and piezoelectric properties. Given that Cr has unpaired *d* electrons, a challenge to overcome in these calculations is the simulation of a truly representative random distribution of the spins of Cr ions, whose placement in the AlN lattice involves not only chemical disordering but also spin disordering. Among a set of wurtzite-based materials, we find that Cr-doped AlN is the alloy whose piezoelectric stress coefficient e_{33} is the most sensitive to alloying concentration and also has the lowest transition composition. The key factor leading to the enhanced piezoelectricity in $Cr_xAl_{1-x}N$ alloys is the ionic contribution to the coefficient e_{33}; this ionic contribution is increased through the internal u parameter of the wurtzite structure when alloyed with the (larger) Cr ions. Therefore, we propose $Cr_xAl_{1-x}N$ as a viable piezoelectric material with properties that can be tuned via Cr composition. To further support this proposal, we perform a combinatorial synthesis and a subsequent characterization of $Cr_xAl_{1-x}N$ films, and we show that Cr can be incorporated into the AlN lattice up to 30% before a detectable transition to rocksalt occurs. At this Cr content, the piezoelectric modulus d_{33} is 4 times larger than that of AlN. Pending future device fabrication and accurate measurements of properties and device performance, this significant increase in d_{33} can propel $Cr_xAl_{1-x}N$ to be the choice material for applications such as resonators, gigahertz telecommunications, or acoustic wave generators.

II. METHODS

A. Paramagnetic representation of $Cr_xAl_{1-x}N$ alloys

Starting with a computational supercell of wurtzite AlN, any desired Cr concentration is realized by substituting a corresponding number of Al ions with Cr ions in the cation sublattice. In order to realistically simulate the chemical disorder of actual $Cr_xAl_{1-x}N$ alloys while maintaining a tractable size for the computational cell, we use special quasirandom structures (SQSs) [21–23]. The Cr^{3+} ions have unpaired *d* electrons which require spin-polarized DFT calculations. Another important aspect of the calculations is that the $Cr_xAl_{1-x}N$ alloys are paramagnetic [19,24,25], and this state has to be captured explicitly in the DFT calculations. Therefore, in addition to the configurational disorder simulated via SQSs, the paramagnetic state requires truly random configurations for the spins associated with the Cr^{3+} ions [26,27]. However, as shown by Abrikosov *et al.* [27], the paramagnetic state can be approximated by using disordered, collinear, static spins because such a state yields zero spin-spin correlation functions. To represent the paramagnetic state of $Cr_xAl_{1-x}N$, for a given alloy structure with n Cr sites, we perform a minimum of $\binom{n}{2}$ and a maximum of 20 calculations. In these calculations, the spins on Cr sites are randomly initialized subject to the restriction of zero total spin for each concentration and each SQS. An example of such a random distribution of initial spins is illustrated in Fig. 1 for the $x = 25\%$ Cr concentration.

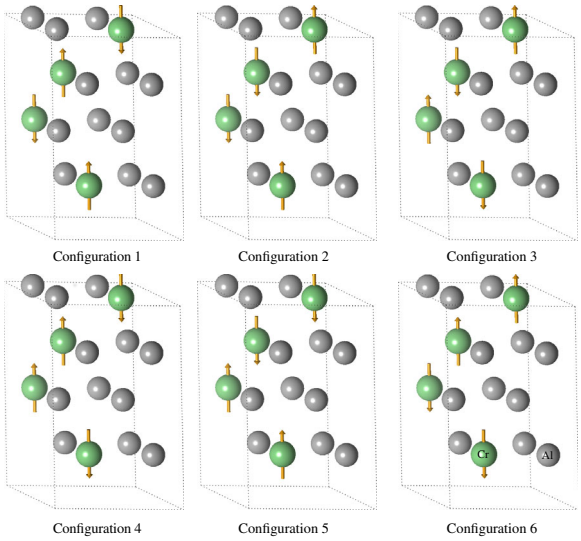

FIG. 1. Schematics of a cation sublattice of a $Cr_xAl_{1-x}N$ alloy. Al (Cr) sites are shown as gray (green) spheres. At a given Cr concentration, the Cr sites of each configuration have a different and random spin initialization with zero total spin in order to capture the paramagnetic state.

B. Details of the DFT calculations

Structural optimizations and calculations of piezoelectric and elastic constants are carried out using the Vienna *ab initio* simulation package [28], with projector augmented waves in the generalized-gradient approximation using the Perdew-Burke-Ernzerhof exchange-correlation function [29] and an on-site Hubbard term U [30] for the Cr 3*d* states. The plane-wave cutoff energy is set to 540 eV in all calculations. For the wurtzite structures, we use $4 \times 4 \times 2$ (128 atoms) and $2 \times 2 \times 2$ (32 atoms) SQS supercells; for the rocksalt structures, the computations are carried out on $2 \times 2 \times 2$ (64 atoms) SQS supercells. Brillouin-zone sampling is performed by employing $1 \times 1 \times 1$ and $2 \times 2 \times 2$ Monkhorst-Pack [31] k-point meshes for the wurtzite and rocksalt structures, respectively, with the origin set at the Γ point in each case. Piezoelectric coefficients are calculated

using density-functional perturbation theory, and the elastic constants are computed by finite differences [32,33]. The on-site Coulomb interaction for Cr atoms is set at 3 eV using the Dudarev approach [30]. Before performing the calculations for elastic and piezoelectric constants, we perform cell shape, volume, and ionic relaxations in order to obtain the equilibrium lattice parameters and ionic positions for each particular Cr concentration and SQS alloy.

C. Experimental procedures

Combinatorial synthesis of the $Cr_xAl_{1-x}N$ films is performed through reactive physical vapor deposition (PVD). Circular aluminum (99.9999%) and chromium (99.999%) metallic targets with 2-in. diameters are arranged at 45° angles measured from the normal to a plasma-cleaned Si(100) substrate inside a custom vacuum system with a base pressure of 5×10^{-6} Torr. Magnetron rf sputtering with a power of 60 W for the aluminum targets and 40 W for the chromium targets is performed at a deposition pressure of 3×10^{-3} Torr, with 8 sccm of argon and 4 sccm of nitrogen, and a substrate temperature of 400 °C. Aluminum glow discharges are oriented opposite to each other, with the chromium target perpendicular to both, resulting in a film library with a compositional range in one direction [34,35]. Each sample library is subdivided into 11 regions across the composition gradient, which are subsequently characterized by x-ray diffraction (XRD) and x-ray fluorescence, performed on a Bruker D8 Discover diffractometer with a 2D area detector in a θ-2θ configuration and a Fischer x-ray spectrometer, respectively.

III. RESULTS AND DISCUSSION

A. Enthalpy of mixing

The enthalpy of mixing as a function of the Cr concentration x, at zero pressure, is defined with respect to the pure wurtzite-AlN and rocksalt-CrN phases via

$$\Delta H_{\mathrm{mix}}(x) = E_{\mathrm{Cr}_x\mathrm{Al}_{1-x}\mathrm{N}} - xE_{\mathrm{Rs\text{-}CrN}} - (1-x)E_{\mathrm{Wz\text{-}AlN}}, \quad (1)$$

where $E_{\mathrm{Cr}_x\mathrm{Al}_{1-x}\mathrm{N}}$, $E_{\mathrm{Rs-CrN}}$, and $E_{\mathrm{Wz-AlN}}$ are the total energies per atom of the SQS alloy, the pure AlN phase, and the pure CrN phase, respectively. The DFT-calculated mixing enthalpies for the wurtzite and rocksalt phases of $Cr_xAl_{1-x}N$ are shown in Fig. 2(a). The wurtzite phase is found to be favorable up to $x = 0.25$, beyond which rocksalt alloys are stable; this wurtzite-to-rocksalt phase transition point is consistent with previous experimental observations and other theoretical predictions [19,20].

We compare the mixing enthalpy of the $Cr_xAl_{1-x}N$ alloys to that of several other common wurtzite-based nitrides [13,15,18,36,37], $Sc_xAl_{1-x}N$, $Y_xAl_{1-x}N$, and $Y_xIn_{1-x}N$, with the results shown in Fig. 2(b). The mixing enthalpies are positive in all cases, meaning that the alloying of AlN or InN with their respective end members

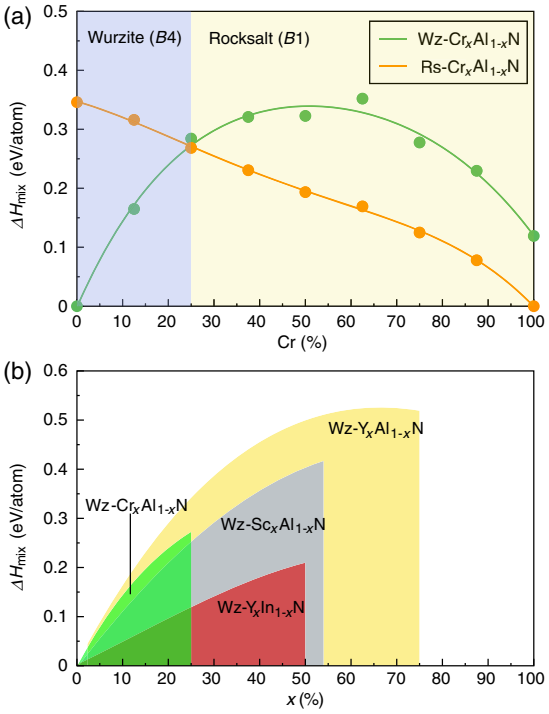

FIG. 2. (a) DFT-calculated mixing enthalpies of the wurtzite and rocksalt phases of $Cr_xAl_{1-x}N$ as functions of the Cr concentration. (b) Calculated mixing enthalpies for several wurtzite-based nitride alloys grown experimentally.

is an endothermic process. In practice, these alloys are formed as disordered solid solutions obtained using physical vapor deposition techniques operating at relatively low substrate temperatures because of the energetic plasmas involved [17,38]. Figure 2(b) shows that the mixing enthalpy in $Cr_xAl_{1-x}N$ lies between values corresponding to other systems synthesized experimentally; hence, $Cr_xAl_{1-x}N$ is no more difficult to synthesize than the others. More importantly, the enthalpy calculations show that the transition to rocksalt occurs at the lowest alloy concentration across the wurtzite systems considered, which is important for achieving maximum piezoresponse-enhancing structural frustration with a minimum of dopant concentration in order to retain the single-phase wurtzite.

B. Piezoelectric stress coefficients

The piezoelectric coefficients e_{ij} for different spin configurations in SQS supercells with the same Cr content are shown in Fig. 3. For clarity, the panels in Fig. 3 are arranged in the same fashion as the piezoelectric tensor when represented as a matrix in Voigt notation. The vertical scale is the same for all coefficients except e_{33}, e_{31}, and e_{32}. The scatter in the results corresponds to different SQS supercells at each Cr concentration; this is an effect of the finite size of the system, in which local distortions around Cr atoms lead to small variations of the lattice constants and angles. It is for this reason that we average the SQS results

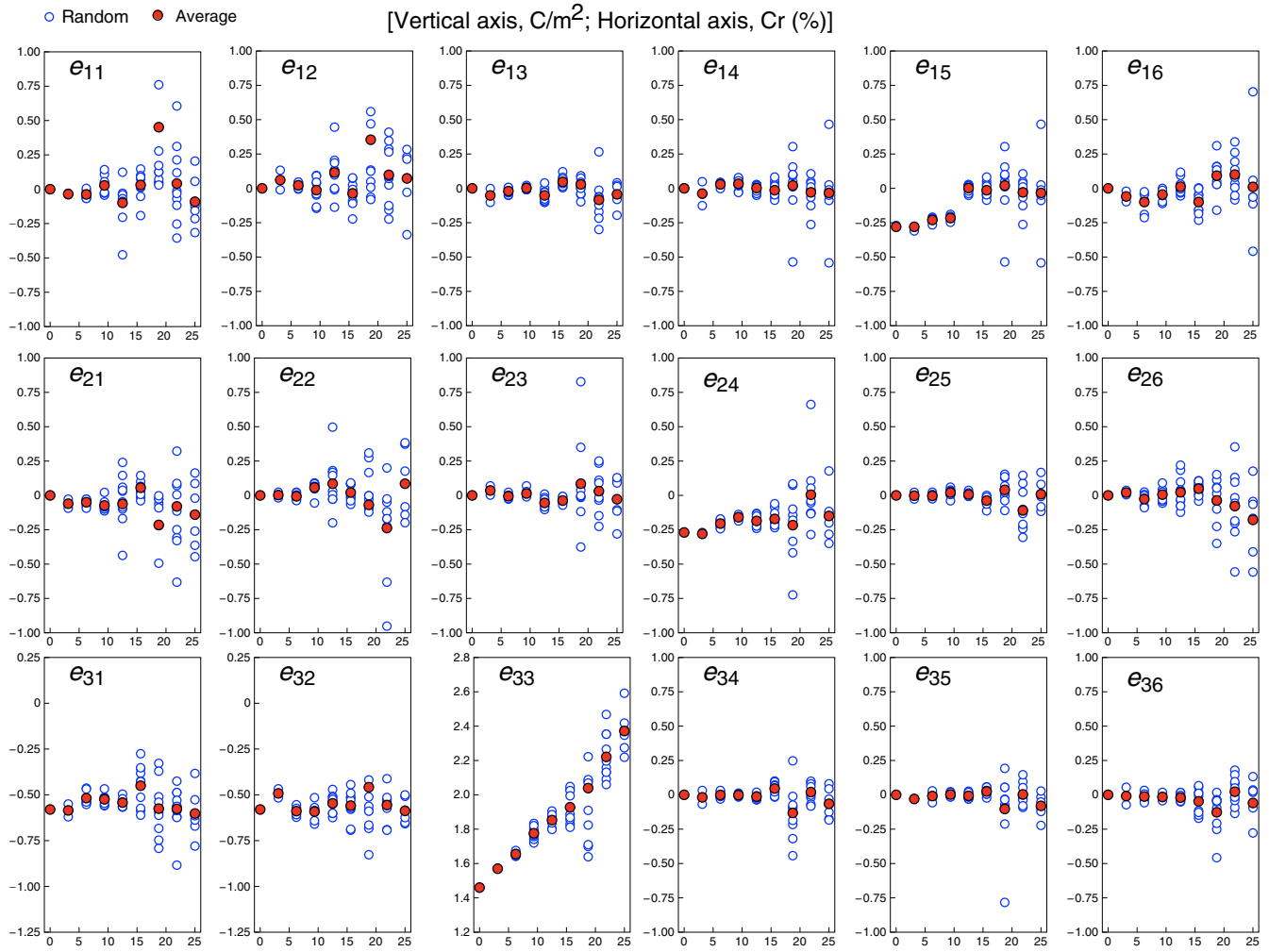

FIG. 3. The 18 components of the piezoelectric tensor calculated for SQS supercells with different spin configurations and compositions of Cr. At each Cr composition, the open circles represent the data for each SQS cell used, while the red solid circles represent the average values across the random initial configurations.

at each Cr concentration, thereby obtaining smoother variations of the piezoelectric coefficients. At 25% Cr, the value of e_{33} becomes about 1.7 times larger than that corresponding to pure AlN.

The piezoelectric coefficient e_{33} of wurtzite $Cr_xAl_{1-x}N$ is shown in Fig. 4(a) as a function of Cr concentration, and it can be written as [39]

$$e_{33}(x) = e_{33}^{\text{clamped}}(x) + e_{33}^{\text{nonclamped}}(x), \tag{2}$$

in which $e_{33}^{\text{clamped}}(x)$ describes the electronic response to strain and is evaluated by freezing the internal atomic coordinates at their equilibrium positions. The term $e_{33}^{\text{nonclamped}}(x)$ is attributed to changes in internal coordinates, and it is given by

$$e_{33}^{\text{nonclamped}}(x) = \frac{4eZ_{33}^{*}(x)}{\sqrt{3}a(x)^2}\frac{du(x)}{d\epsilon}, \tag{3}$$

where e is the (positive) electron charge, $a(x)$ is the equilibrium lattice constant, $u(x)$ is the internal parameter of the wurtzite, $Z_{33}^{*}(x)$ is the dynamical Born charge in units of e, and ϵ is the macroscopic applied strain. $e_{33}^{\text{nonclamped}}(x)$ describes the piezoelectric response coming from the displacements of internal atomic coordinates produced by the macroscopic strain. Based on Eqs. (2) and (3), Figs. 4(b)–4(f) show the different relevant quantities contributing to e_{33} in order to identify the main factors responsible for the increase of piezoelectric response with a Cr addition. Direct inspection of Figs. 4(a)–4(c) indicates that the main contribution to the increase in e_{33} comes from the nonclamped ionic part, Fig. 4(c). Since the Born charge Z_{33}^{*} [Fig. 4(d)] is practically constant, the key factor that leads to increasing the piezoelectric coefficient is the strain sensitivity $du/d\epsilon$ of the internal parameter u [Fig. 4(e)].

Although the internal parameter u is an average value across the entire supercell, the individual average u parameters can also be determined separately for AlN

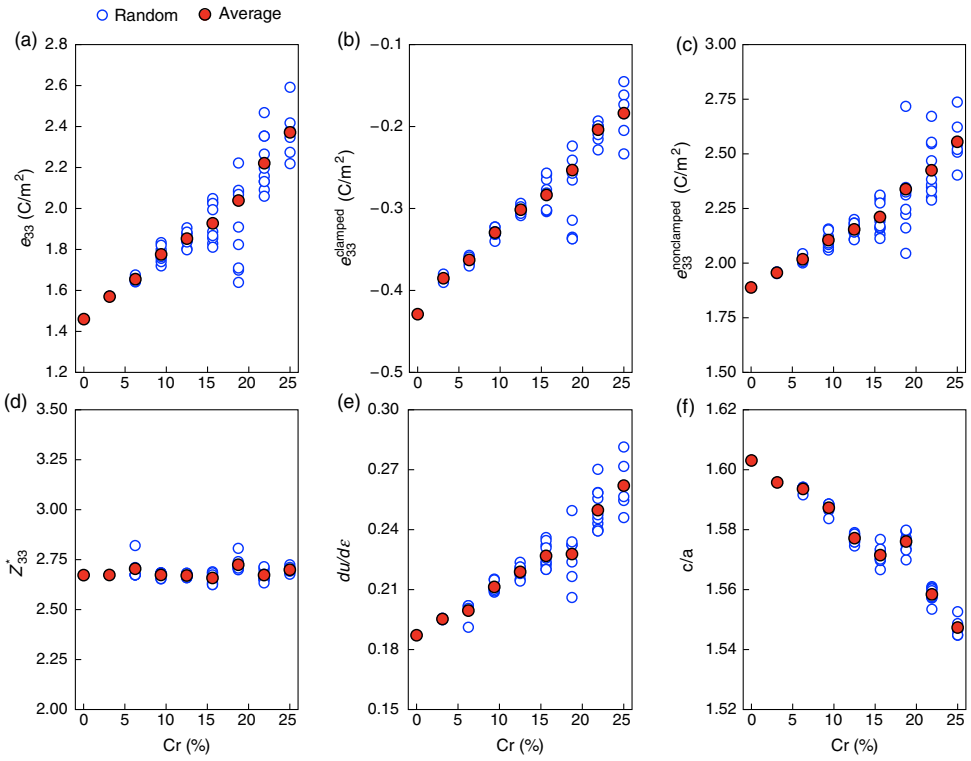

FIG. 4. Variation of (a) e_{33}^{total}, (b) the $e_{33}^{clamped}$ component of e_{33}, (c) $e_{33}^{nonclamped}$, (d) the 33 component of the Born effective charge tensor, (e) the strain sensitivity of the internal parameter, and (f) the c/a ratio with respect to the Cr addition.

and CrN tetrahedra [Figs. 5(a) and 5(b)]. The internal parameter u of the AlN tetrahedra [Fig. 5(b)] does not change significantly, while that of the CrN tetrahedra grows approximately linearly with the Cr concentration [Fig. 5(a)]. In an alloy system where AlN tetrahedra are the majority, this variation can be understood based on (i) the fact that the ionic radius of Cr is about 10% larger than that of Al, and (ii) the increase in Cr concentration will lead to average u parameters mimicking the variation of the u parameter corresponding to the CrN tetrahedra.

C. Comparison with other wurtzite-based alloys

The results from calculations of the piezoelectric properties of $Cr_xAl_{1-x}N$ with x from 0% to 25% Cr are plotted in Fig. 6, together with the calculated values for $Sc_xAl_{1-x}N$, $Y_xAl_{1-x}N$, and $Y_xIn_{1-x}N$. In $Cr_xAl_{1-x}N$, e_{33} increases rapidly from 1.46 to 2.40 C/m^2 for Cr concentrations ranging from 0% to 25%. For all of the other alloys considered, the increase is smaller in the same interval of solute concentration: for $Sc_xAl_{1-x}N$, $Y_xAl_{1-x}N$, and $Y_xIn_{1-x}N$, e_{33} increases, respectively, from 1.55 to 1.9 C/m^2, 1.55 to 1.7 C/m^2, and 0.9 to 1.2 C/m^2.

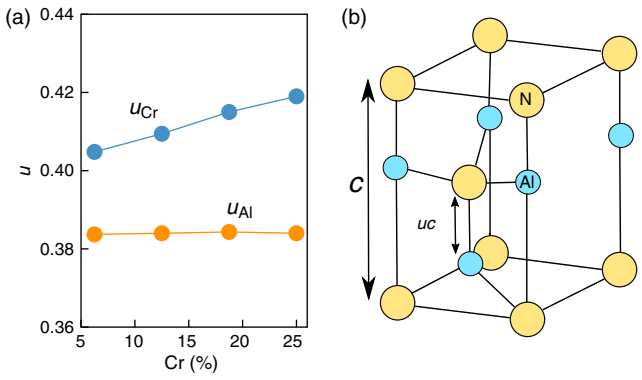

FIG. 5. (a) Variation of the internal parameter, u, with the Cr addition. (b) Crystal structure of wurtzite AlN.

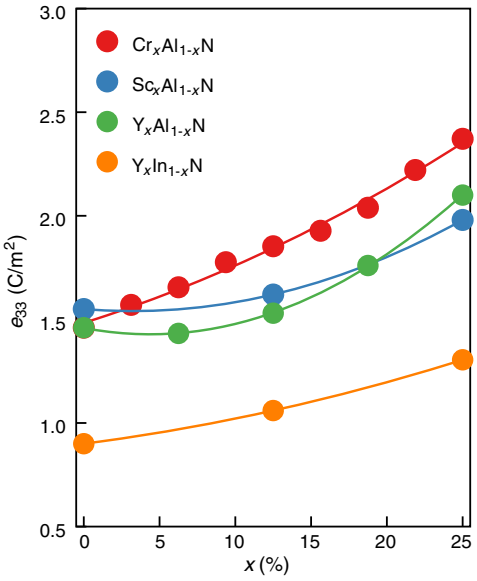

FIG. 6. Comparison of change in e_{33} with the addition of different transition metals for the $x \leq 25\%$ regime.

Within the $x \leq 25\%$ range, Cr is more effective than any of the other studied transition elements in improving the piezoelectric response of AlN-based alloys.

The experimentally measurable property is d_{33}, which is commonly known as the piezoelectric strain modulus and relates the electric polarization vector with stress. The relationship between the piezoelectric strain and stress moduli is [40]

$$d_{ij} = \sum_{k=1}^{6} e_{ik}(C^{-1})_{kj}, \tag{4}$$

where C_{ij} represents the elements of the stiffness tensor in Voigt notation. The variation of the elastic constant C_{33} in $Cr_xAl_{1-x}N$ with x is shown in Fig. 7(a), along with the other systems considered here. For all of these wurtzite-based piezoelectrics, the increase in piezoelectric response with the alloying element concentration is accompanied by mechanical softening (a decrease in C_{33}). From Eq. (4), it follows that the increase in e_{33} (Fig. 6) and the mechanical softening [Fig. 7(a)] cooperate to lead to the increase of d_{33} values with alloy concentration x. Our calculated d_{33} values for $Cr_xAl_{1-x}N$ are in good agreement with the experimental data from Ref. [38] [Fig. 7(b)] for Cr concentrations of up to 6.3%. Beyond this concentration, Luo *et al.* [38] reported a drop in the d_{33} values of their films which was attributed to changes in the film texture. We also extend our calculations of piezoelectric coefficients beyond 25% Cr composition in wurtzite structures. Figure 8 shows that e_{33} continues to increase at least up to 37.5% Cr. The calculations done at 50% Cr, which start with wurtzite SQS configurations, evolve into rocksalt configurations during relaxation, which explains the decrease of e_{33} to zero in Fig. 8.

It is worthwhile to compare the performance of several AlN wurtzite-based materials for their use in applications. These applications, which are mainly resonators, ultrasound wave generators, gigahertz telecommunications, film bulk acoustic resonator devices, bulk or surface acoustic generators, and biosensors, lead to a multitude of application-specific figures of merit for different utilization modes of the piezoelectric material. However, most figures of merit rely on the piezoelectric properties e_{33} and d_{33}, both of which, in general, should be as large as possible for increased piezoelectric device sensitivity. The most used wurtzite material for these applications is AlN, although there are several other options as well (see Table I). Alloying with ScN is promising in that it offers an increased d_{33} value for concentrations of about 10% Sc; larger Sc concentrations are possible, but the growth process becomes more costly and the material is likely to lose texture with an increased Sc content. Options such as alloying with YN offer marginal improvement at 6% Y content, and YN-doped InN (14% Y content) fares similarly (Table I). Our results indicate that CrN alloying of AlN leads to superior values for the piezoelectric properties, nearly quadrupling the value of d_{33} (Table I) with respect to AlN. The fact that the transition point is the

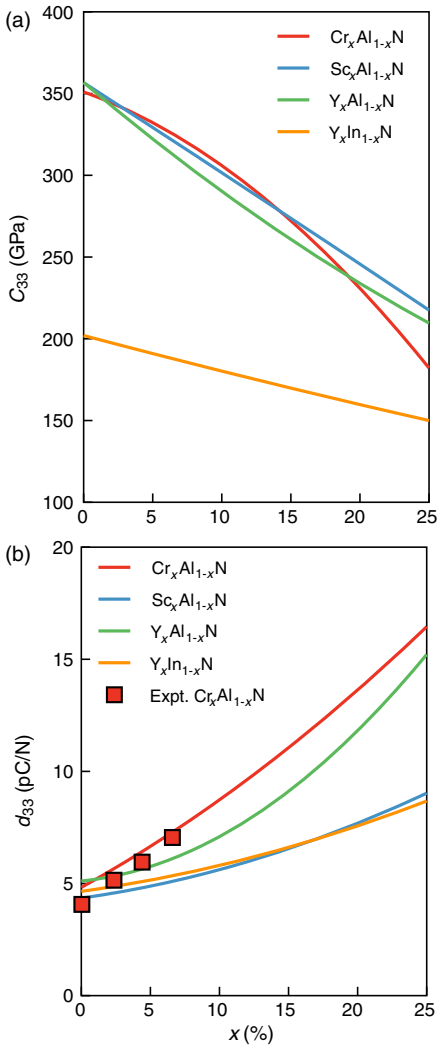

FIG. 7. Variation of (a) C_{33} and (b) d_{33} for several nitride-based wurtzite alloys.

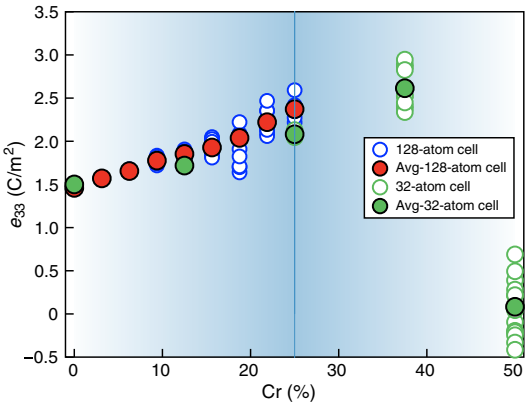

FIG. 8. Variation of e_{33} as a function of Cr concentration for wurtzite phase alloys of up to 50%.

TABLE I. Piezoelectric properties of AlN and a few wurtzite alloys for piezoelectric device applications.

Material	e_{33} (C/m^2)	d_{33} (pC/N)	Ref(s).
AlN	1.55	4.5–5.3	[1,2,10]
$Sc_xAl_{1-x}N$, 10% Sc	1.61	7.8	[41,42]
$Y_xAl_{1-x}N$, 6% Y	1.5	4.0	[18]
$Y_xIn_{1-x}N$, 14% Y	1.1	5.1	[36]
This work			
$Cr_xAl_{1-x}N$, 12.5% Cr	1.84	9.86	
$Cr_xAl_{1-x}N$, 25.0% Cr	2.35	16.45	
$Cr_xAl_{1-x}N$, 30.0% Cr	2.59	19.52	

lowest (Fig. 2) of all wurtzite-based materials relevant for the technologies mentioned above makes the CrN alloying easier than with the other materials (which require higher alloy content) and hence renders $Cr_xAl_{1-x}N$ a prime candidate for the synthesis of future, CrN-alloyed piezoelectrics for resonators and acoustic generators. As we see in Sec. III D, nonequilibrium growth techniques can bring Cr content past the transition point without significant formation of the (nonpiezoelectric) rocksalt phase. Consequently, the piezoelectric properties are expected to be significantly better than those of AlN, especially d_{33} (see Table I). Indeed, this is borne out in experiments [the data points in Fig. 7(b)]. Measurements of figures of merit for specific device configurations will be needed in the future, as they require not only combinations of elastic and piezoelectric properties, but also dielectric properties [15].

D. Experimental results

To bring experimental support to our proposal that the $Cr_xAl_{1-x}N$ system can become a key piezoelectric material to replace AlN and perhaps even ZnO for future applications, we have to ensure that the texture obtained during growth is stable for sufficiently high CrN concentrations. After synthesizing $Cr_xAl_{1-x}N$ alloys through reactive PVD, we perform a transmission-electron-microscopy (TEM) analysis of the films grown in order to check for textural integrity (i.e., grains oriented primarily with the c axis close to the surface normal) and for the onset of the rocksalt phase. At CrN content below 25% [the theoretical boundary shown in Fig. 2(a)], our films display no significant texture variations. For example, Fig. 9(a) shows a typical TEM micrograph wherein the texture is preserved over the film thickness. Additionally, our energy-dispersive spectroscopy (EDS) characterization shows nearly constant Cr content through the sample [Fig. 9(b)]. Further characterization by XRD is performed for all CrN compositions in the combinatorially synthesized films. Figure 10 shows the XRD results for the 88 discrete $Cr_xAl_{1-x}N$ compositions produced in an effort to test the possibilities of synthesizing alloys in a wide range of concentrations, including alloys

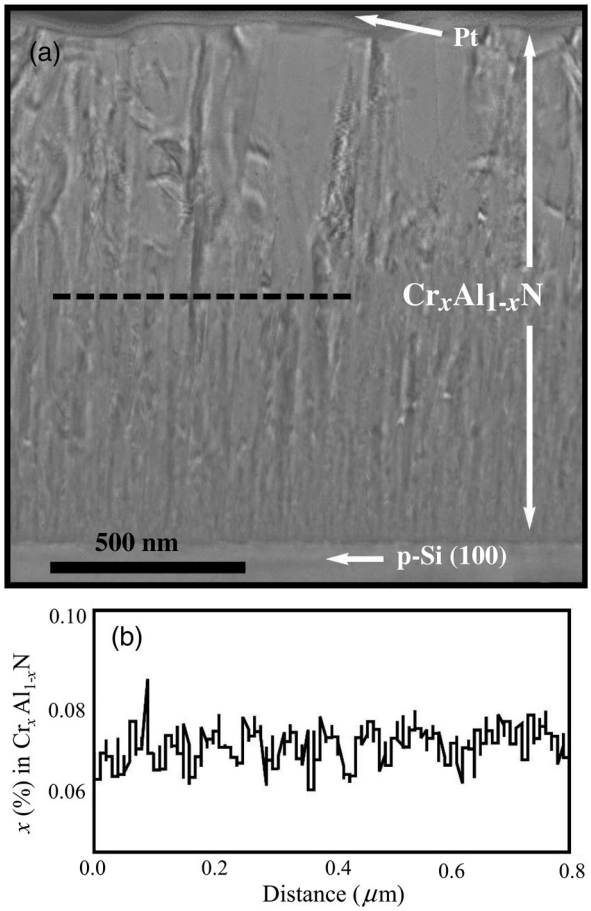

FIG. 9. (a) Representative TEM image and (b) an EDS line scan of an $Cr_xAl_{1-x}N$ film cross section containing approximately 7% Cr, confirming the incorporation of Cr into the wurtzite solid solution. EDS data are collected along the dashed black line shown in (a).

beyond the wurtzite-to-rocksalt transition point. At low alloying levels, the films grow exclusively with the wurtzite structure and a (002) preferred orientation, as indicated by the dominant presence of the wurtzite (002) diffraction peak (Fig. 10, left-hand side). Films grown by reaction PVD under the conditions used here accept chromium into the wurtzite lattice and grow primarily with the ideal (002) orientation. With an increased CrN content, the wurtzite (012) and (010) peaks appear, indicating some deviations from the original, and still display a predominant (002) orientation of the film. The metastability of this alloy is overcome at an approximate composition of $x \simeq 30\%$, where the polycrystalline rocksalt phase appears, as revealed by the rocksalt (002) and (111) peaks (Fig. 10, right-hand side). These experimental results show that wurtzite $Cr_xAl_{1-x}N$ solid solutions can be synthesized without observable phase separation up to concentrations of 30% Cr. Wurtzite material still exists at global compositions beyond 30%, but in a wurtzite-rocksalt phase mixture, which will diminish the piezoelectric properties

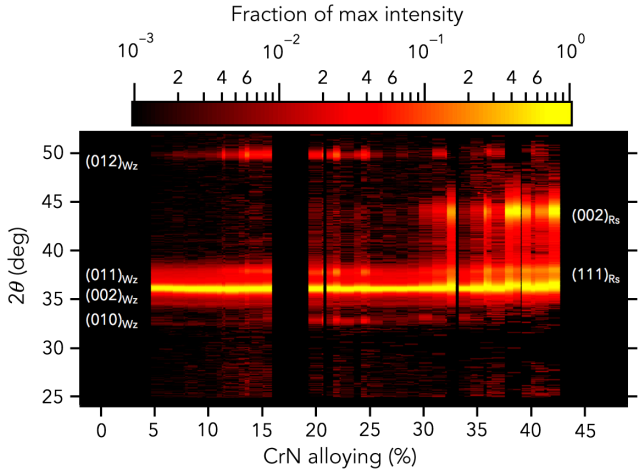

FIG. 10. X-ray diffraction patterns of the thin-film combinatorial libraries plotted against the film composition, with comparison to the patterns for wurtzite (Wz) [43] and rocksalt (Rs) [44] structures. For alloying content $x < 30\%$, the films grow predominantly with the wurtzite structure. At higher Cr concentrations, $x > 30\%$, both the rocksalt and wurtzite phases are detected, and the wurtzite exhibits a degraded texture. No films are produced with compositions in regions where no intensity is shown.

because of the presence of a significant amount of centrosymmetric rocksalt phase in the mixture.

There were a few studies of Cr alloyed into wurtzite AlN [25,38,45] reporting Cr-doped alloys grown by magnetron sputtering. The Cr concentration previously attained is below 10%, although the limits of Cr alloying were not actually tested in the previous reports [25,38,45]. Our combinatorial synthesis results show that Cr can be doped into the wurtzite lattice up to 11% before the predominant (002) film texture starts to change, and up to 30% before the rocksalt phase appears.

IV. CONCLUDING REMARKS

By using a physical representation of the paramagnetic state of substitutional Cr in a wurtzite AlN matrix and performing the necessary averaging over spin configurations at each Cr concentration, we compute the structural, mechanical, and piezoelectric properties of $Cr_xAl_{1-x}N$ alloys. Our combinatorial synthesis experiments show that $Cr_xAl_{1-x}N$ is relatively easy to synthesize, and they also show that the reactive PVD procedure results in $Cr_xAl_{1-x}N$ alloys retaining the wurtzite structure for alloying concentrations up to 30% Cr. Remarkably, our DFT calculations of piezoelectric properties reveal that, for 12.5% Cr, d_{33} is twice that of pure AlN and that, for 30% Cr, this modulus is about 4 times larger than that of AlN.

From a technological standpoint, this finding should make $Cr_xAl_{1-x}N$ the prime candidate to replace the current wurtzite-based materials in resonators and acoustic wave generators. The larger (than AlN) piezoelectric response may lead to reduced power consumption—and perhaps even to avenues to further miniaturize various devices. While the substitutional alloying with Cr would improve the piezoelectric response for every type of device in which AlN is currently being used, one may wonder why alloying with other trivalent metals is not pursued. In particular, Sc has been shown to significantly increase the piezoelectric modulus as well [16]. Even though $Sc_xAl_{1-x}N$ has more exciting properties than $Cr_xAl_{1-x}N$ [14,16], the reason why ScN alloys have not taken over the resonator market is that the outstanding enhancements in piezoelectric properties occur at very high Sc concentrations (Fig. 2; $x > 55\%$), at which the stability of the wurtzite phase is rather poor. $Cr_xAl_{1-x}N$ has a low wurtzite-to-rocksalt transition concentration, and it therefore can offer certain piezoelectric enhancements at alloying levels that are easier to stabilize during the synthesis.

In order to ensure a significant impact of $Cr_xAl_{1-x}N$ alloys as materials to outperform and replace the established piezoelectrics AlN and ZnO, two avenues should be pursued in the near future. First, to benefit from the 300% increase in d_{33} at 30% Cr content, it is not sufficient that the rocksalt phase does not form up to that Cr concentration: we also have to avoid the formation of (012)- and (010)-oriented grains during growth, which would downgrade (simply through directional averaging) the piezoelectric enhancements associated with the (002)-oriented grains. To that end, we envision changing substrates so as to enable better lattice matching with Cr alloys having over 25% Cr. Such lattice matching can effectively prevent the (012) and (010) textures from emerging, therefore creating the conditions to take advantage of the large increase in d_{33} reported here. Second, future experimental efforts should measure device performance, especially to understand the additional aspect of how Cr content in wurtzite affects the band gap and whether there would be deleterious leakage effects at larger Cr concentrations. Assuming a worst-case scenario, these effects can be mitigated by coalloying with a nonmetallic end member.

Pursuing the two directions above can make $Cr_xAl_{1-x}N$ suitable for simultaneous optical and mechanical resonators [46,47], which are relatively recent applications that currently exploit multiphysics aspects of AlN. At present, the characterization of $Cr_xAl_{1-x}N$ for those multifunctional applications that require the simultaneous engineering of the photonic and acoustic band structure is rather incipient, and only a few relevant properties of the $Cr_xAl_{1-x}N$ alloys are known: for example, for a Cr concentration of about 2%, the band gap is virtually unchanged, while the adsorption band decreases from 6 to 3.5 eV [48]. Future theoretical and experimental work to investigate, e.g., the photoelastic effect and optical attenuation, is necessary in order to fully uncover the potential for Cr-doped AlN in these applications. For now, we surmise that the technological reason for which one would replace AlN with

$Cr_xAl_{1-x}N$ for use in multifunctional resonators is the trade-off between the increase in vibrational amplitude and the decrease in frequency: while low amounts of Cr may lower the frequency somewhat, the oscillation amplitude would increase due to a larger piezoelectric response. The decrease in frequency can be mitigated by codoping with a small trivalent element (boron), as shown for other doped AlN alloys [15]. Last but not least, it is worth noting that doping with Cr could enable magnetic polarizaton of the Cr ions in the wurtzite lattice and/or of the minority carriers: these effects are nonexistent in pure AlN, and they could be pursued for spintronic applications or for low-hysteresis magnets [25].

The significant increase in the piezoelectric modulus reported here provides a impetus to pursue the two directions identified above, and to overcome routine barriers towards establishing $Cr_xAl_{1-x}N$ as a replacement for AlN with large performance enhancements.

ACKNOWLEDGMENTS

The authors gratefully acknowledge the support of the National Science Foundation through Grant No. DMREF-1534503. The DFT calculations were performed using the high-performance computing facilities at the Colorado School of Mines (the Golden Energy Computing Organization) and at the National Renewable Energy Laboratory (NREL). Synthesis and characterization facilities at NREL were supported by the U.S. Department of Energy, Office of Science, Office of Basic Energy Sciences, as part of the Energy Frontier Research Center "Center for Next Generation of Materials by Design: Incorporating Metastability," under Contract No. DE-AC36-08GO28308.

[1] Y. Q. Fu, J. K. Luo, N. T. Nguyen, A. J. Walton, A. J. Flewitt, X. T. Zu, Y. Li, G. McHale, A. Matthews, E. Iborra, H. Du, and W. I. Milne, Advances in piezoelectric thin films for acoustic biosensors, acoustofluidics and lab-on-chip applications, Prog. Mater. Sci. **89**, 31 (2017).

[2] P. Muralt, Recent progress in materials issues for piezoelectric MEMS, J. Am. Ceram. Soc. **91**, 1385 (2008).

[3] H. Loebl, M. Klee, C. Metzmacher, W. Brand, R. Milsom, and P. Lok, Piezoelectric thin AlN films for bulk acoustic wave (BAW) resonators, Mater. Chem. Phys. **79**, 143 (2003).

[4] F. Gerfers, M. Kohlstadt, H. Bar, M.-Y. He, Y. Manoli, and L.-P. Wang, in *Proceedings of the Solid-State Sensors, Actuators and Microsystems Conference (TRANSDUCERS 2007), Lyon, France, 2007* (IEEE, New York, 2007), p. 1191.

[5] Y. Wang, H. Ding, X. Le, W. Wang, and J. Xie, A MEMS piezoelectric in-plane resonant accelerometer based on aluminum nitride with two-stage microleverage mechanism, Sens. Actuators **254**, 126 (2017).

[6] C. Zuo, J. Van der Spiegel, and G. Piazza, 1.05-GHz CMOS oscillator based on lateral-field-excited piezoelectric AlN contour- mode MEMS resonators, IEEE Trans. Ultrason. Ferroelectr. Freq. Control **57**, 82 (2010).

[7] N. Wang, C. Sun, L. Y. Siow, H. Ji, P. Chang, Q. Zhang, and Y. Gu, in *Proceedings of the IEEE 30th International Conference on Micro Electro Mechanical Systems (MEMS), Las Vegas, 2017* (IEEE, New York, 2017), p. 841.

[8] R. Elfrink, T. Kamel, M. Goedbloed, S. Matova, D. Hohlfeld, Y. Van Andel, and R. Van Schaijk, Vibration energy harvesting with aluminum nitride-based piezoelectric devices, J. Micromech. Microeng. **19**, 094005 (2009).

[9] C.-M. Yang, K. Uehara, S.-K. Kim, S. Kameda, H. Nakase, and K. Tsubouchi, in *Proceedings of the IEEE Symposium on Ultrasonics, Honolulu, 2003* (IEEE, New York, 2003), p. 170.

[10] P. Muralt, in *Piezoelectric MEMS Resonators*, edited by H. Bhugra and G. Piazza, Microsystems and Nanosystems (Springer International Publishing, Cham, Switzerland, 2017), p. 3.

[11] By convention, we refer to the e_{ij} values, which couple strain and dielectric displacement (or electric field and stress), as piezoelectric coeffcients, while the d_{ij} values, which couple strain with electric field (or stress with dielectric displacement), are referred to as piezoelectric moduli. In both cases, we express the individual matrix elements in standard reduced Voigt notation.

[12] X. Kang, S. Shetty, L. Garten, J. F. Ihlefeld, S. Trolier-McKinstry, and J.-P. Maria, Enhanced dielectric and piezoelectric responses in $Zn_{1-x}Mg_xO$ thin films near the phase separation boundary, Appl. Phys. Lett. **110**, 042903 (2017).

[13] M. Akiyama, T. Kamohara, K. Kano, A. Teshigahara, Y. Takeuchi, and N. Kawahara, Enhancement of piezoelectric response in scandium aluminum nitride alloy thin films prepared by dual reactive cosputtering, Adv. Mater. **21**, 593 (2009).

[14] M. A. Caro, S. Zhang, T. Riekkinen, M. Ylilammi, M. A. Moram, O. Lopez-Acevedo, J. Molarius, and T. Laurila, Piezoelectric coefficients and spontaneous polarization of ScAlN, J. Phys. Condens. Matter **27**, 245901 (2015).

[15] S. Manna, G. L. Brennecka, V. Stevanović, and C. V. Ciobanu, Tuning the piezoelectric and mechanical properties of the AlN system via alloying with YN and BN, J. Appl. Phys. **122**, 105101 (2017).

[16] F. Tasnádi, B. Alling, C. Höglund, G. Wingqvist, J. Birch, L. Hultman, and I. A. Abrikosov, Origin of the Anomalous Piezoelectric Response in Wurtzite $Sc_xAl_{1-x}N$ Alloys, Phys. Rev. Lett. **104**, 137601 (2010).

[17] C. Höglund, J. Birch, B. Alling, J. Bareño, Z. Czigány, P. O. Persson, G. Wingqvist, A. Žukauskaitė, and L. Hultman, Wurtzite structure $Sc_{1-x}Al_xN$ solid solution films grown by reactive magnetron sputter epitaxy: Structural characterization and first-principles calculations, J. Appl. Phys. **107**, 123515 (2010).

[18] P. M. Mayrhofer, H. Riedl, H. Euchner, M. Stöger-Pollach, P. H. Mayrhofer, A. Bittner, and U. Schmid, Microstructure and piezoelectric response of $Y_xAl_{1-x}N$ thin films, Acta Mater. **100**, 81 (2015).

[19] P. Mayrhofer, D. Music, T. Reeswinkel, H.-G. Fu, and J. Schneider, Structure, elastic properties and phase stability of $Cr_{1-x}Al_xN$, Acta Mater. **56**, 2469 (2008).

[20] D. Holec, F. Rovere, P. H. Mayrhofer, and P. B. Barna, Pressure-dependent stability of cubic and wurtzite phases within the TiN-AlN and CrN-AlN systems, Scr. Mater. **62**, 349 (2010).

[21] A. Zunger, S.-H. Wei, L. G. Ferreira, and J. E. Bernard, Special Quasirandom Structures, Phys. Rev. Lett. **65**, 353 (1990).

[22] A. van de Walle, Multicomponent multisublattice alloys, nonconfigurational entropy and other additions to the alloy theoretic automated toolkit, CALPHAD: Comput. Coupling Phase Diagrams Thermochem. **33**, 266 (2009).

[23] A. Van de Walle, P. Tiwary, M. De Jong, D. Olmsted, M. Asta, A. Dick, D. Shin, Y. Wang, L.-Q. Chen, and Z.-K. Liu, Efficient stochastic generation of special quasirandom structures, CALPHAD: Comput. Coupling Phase Diagrams Thermochem. **42**, 13 (2013).

[24] Y. Endo, T. Sato, Y. Kawamura, and M. Yamamoto, Crystal structure and magnetic properties of Cr-doped AlN films with various Cr concentrations, Mater. Trans., JIM **48**, 465 (2007).

[25] Y. Endo, T. Sato, A. Takita, Y. Kawamura, and M. Yamamoto, Magnetic, electrical properties, and structure of Cr-AlN and Mn-AlN thin films grown on Si substrates, IEEE Trans. Magn. **41**, 2718 (2005).

[26] B. Alling, T. Marten, and I. Abrikosov, Effect of magnetic disorder and strong electron correlations on the thermodynamics of CrN, Phys. Rev. B **82**, 184430 (2010).

[27] I. Abrikosov, A. Ponomareva, P. Steneteg, S. Barannikova, and B. Alling, Recent progress in simulations of the paramagnetic state of magnetic materials, Curr. Opin. Solid State Mater. Sci. **20**, 85 (2016).

[28] G. Kresse and J. Furthmüller, Efficiency of ab-initio total energy calculations for metals and semiconductors using a plane-wave basis set, Comput. Mater. Sci. **6**, 15 (1996).

[29] J. P. Perdew, K. Burke, and M. Ernzerhof, Generalized Gradient Approximation Made Simple, Phys. Rev. Lett. **77**, 3865 (1996).

[30] S. Dudarev, G. Botton, S. Savrasov, C. Humphreys, and A. Sutton, Electron-energy-loss spectra and the structural stability of nickel oxide: An LSDA + U study, Phys. Rev. B **57**, 1505 (1998).

[31] H. J. Monkhorst and J. D. Pack, Special points for Brillouin-zone integrations, Phys. Rev. B **13**, 5188 (1976).

[32] X. Gonze and C. Lee, Dynamical matrices, born effective charges, dielectric permittivity tensors, and interatomic force constants from density-functional perturbation theory, Phys. Rev. B **55**, 10355 (1997).

[33] X. Wu, D. Vanderbilt, and D. Hamann, Systematic treatment of displacements, strains, and electric fields in density-functional perturbation theory, Phys. Rev. B **72**, 035105 (2005).

[34] A. W. Welch, L. L. Baranowski, P. Zawadzki, S. Lany, C. A. Wolden, and A. Zakutayev, $CuSbSe_2$ photovoltaic devices with 3% efficiency, Appl. Phys. Express **8**, 082301 (2015).

[35] A. W. Welch, L. L. Baranowski, H. Peng, H. Hempel, R. Eichberger, T. Unold, S. Lany, C. A. Wolden, and A. Zakutayev, Trade-offs in thin film solar cells with layered chalcostibite photovoltaic absorbers, Adv. Energy Mater. **7**, 1601935 (2017).

[36] C. Tholander, J. Birch, F. Tasnádi, L. Hultman, J. Palisaitis, P. O. Å. Persson, J. Jensen, P. Sandström, B. Alling, and A. Žukauskaitė, *Ab initio* calculations and experimental study of piezoelectric $Y_xIn_{1-x}N$ thin films deposited using reactive magnetron sputter epitaxy, Acta Mater. **105**, 199 (2016).

[37] A. Žukauskaitė, C. Tholander, J. Palisaitis, P. O. Å. Persson, V. Darakchieva, N. B. Sedrine, F. Tasnádi, B. Alling, J. Birch, and L. Hultman, $Y_xAl_{1-x}N$ thin films, J. Phys. D **45**, 422001 (2012).

[38] J. Luo, B. Fan, F. Zeng, and F. Pan, Influence of Cr-doping on microstructure and piezoelectric response of AlN films, J. Phys. D **42**, 235406 (2009).

[39] F. Bernardini, V. Fiorentini, and D. Vanderbilt, Spontaneous polarization and piezoelectric constants of III-V nitrides, Phys. Rev. B **56**, R10024 (1997).

[40] J. F. Nye, *Physical Properties of Crystals: Their Representation by Tensors and Matrices* (Oxford University Press, New York, 1985).

[41] R. Matloub, A. Artieda, C. Sandu, E. Milyutin, and P. Muralt, Electromechanical properties of $Al_{0.9}Sc_{0.1}N$ thin films evaluated at 2.5 GHz film bulk acoustic resonators, Appl. Phys. Lett. **99**, 092903 (2011).

[42] G. Wingqvist, F. Tasnádi, A. Žukauskaitė, J. Birch, H. Arvin, and L. Hultman, Increased electromechanical coupling in w-$Sc_xAl_{1-x}N$, Appl. Phys. Lett. **97**, 112902 (2010).

[43] M. N. Eddine, E. Bertaut, M. Roubin, and J. Paris, Crystallographic study on low-temperature $Cr_{1-x}V_xN$, Acta Crystallogr. Sect. B **33**, 3010 (1977).

[44] R. W. G. Wyckoff and R. W. Wyckoff, *Crystal Structures*, Vol. 2 (Interscience, New York, 1960).

[45] V. V. Felmetsger and M. K. Mikhov, in *Proceedings of the 2011 IEEE International Ultrasonics Symposium (IUS), Orlando, 2011* (IEEE, New York, 2011), p. 835.

[46] L. R. Fan, X. K. Sun, C. Xiong, C. Schuck, and H. X. Tang, Aluminum nitride piezo-acousto-photonic crystal nanocavity with high quality factors, Appl. Phys. Lett. **102**, 153507 (2013).

[47] C. Xiong, L. R. Fan, X. K. Sun, and H. X. Tang, Cavity piezooptomechanics: Piezoelectrically excited, optically transduced optomechanical resonators, Appl. Phys. Lett. **102**, 021110 (2013).

[48] A. Y. Polyakov, N. B. Smirnov, A. V. Govorkov, R. M. Frazier, J. Y. Liefer, G. T. Thaler, C. R. Abernathy, S. J. Pearton, and J. M. Zavada, Properties of highly Cr-doped AlN, Appl. Phys. Lett. **85**, 4067 (2004).